Numerical Simulation of In-situ Oil Shale Extraction via Electrical Resistance Heating

Guangshuo Fu, Yudou Wang *

School of Science, China University of Petroleum (East China), Qingdao, 266580, China

Abstract. Conventional heating methods for oil shale extraction are limited by restricted heating ranges and uneven temperature distribution. This study explores the feasibility of applying electrical resistance heating to oil shale production. The in-situ extraction process involves complex chemical reactions, multiphase flow, and pore evolution. To account for these factors, we developed a mathematical model that integrates the electric field, heat transfer, chemical reactions, and mass transfer. This model simulates the distribution of electrical energy and temperature within the formation, as well as kerogen decomposition and production efficiency under electric heating conditions. The results show that electrical resistance heating provides a more uniform temperature distribution, making it an effective method for oil shale extraction. Moreover, the numerical model serves as a valuable tool for evaluating and optimizing production strategies using this approach.

Keywords: Oil Shale; Resistance Heating; Kerogen Pyrolysis; Numerical Simulation.

1. Introduction

The development of unconventional oil and gas reservoirs has attracted significant global attention. Oil shale, a sedimentary rock rich in organic matter, can generate oil and gas through thermal decomposition (pyrolysis) [1]. Current global oil shale reserves are estimated to be as high as 410 billion tons, highlighting oil shale's substantial potential for development and utilization [2].

Several in-situ heating methods have been proposed for oil shale extraction, including Shell′s In-situ Conversion Process (ICP) [3], Chevron′s CRUSH technology [4], and Texas A&M′s Steamfrac method [5]. However, these techniques primarily rely on heat conduction or convection, and due to oil shale′s low thermal conductivity and permeability, their heating efficiency remains suboptimal. In recent times, radiation-based heating methods have surfaced as a viable alternative. Zhang et al. [6] conducted numerical simulations comparing various heating methods to evaluate their effectiveness. Zhu et al. [7] proposed an intermittent microwave heating approach and assessed its performance through simulation. Similarly, Ramsay [8] explored the feasibility of radio-frequency heating for oil shale, demonstrating its potential applications.

Beyond these conventional methods, electrical resistance heating (ERH) has shown promise in efficiently elevating subsurface temperatures. Bera et al. [9] compared the heating efficiency and shale oil recovery performance of resistive heating with hydrothermal methods through simulations and experiments, finding ERH to be more effective for enhancing heavy oil recovery. Wang et al. [10] experimentally validated the feasibility of ERH for gas reservoir exploitation. In shale oil extraction, an electro-heating approach integrated with hydraulic fracturing was pioneered by Symington et al. [11], who also carried out successful field tests. ERH has also been employed in soil remediation, where Martin et al. [12] demonstrated its effectiveness in removing trichloroethylene (TCE) from contaminated soil. Wang et al. [13] developed an electro-heating method to enhance shale gas desorption, investigating the impact of reservoir and electrode parameters on heating efficiency.

Many studies substitute heating wells with constant-temperature heat sources in their models [14]. Yang et al. [15] used MATLAB′s PDE toolbox to simulate the temperature distribution of resistive heaters and conducted orthogonal experimental analysis to evaluate the influence of various factors. However, their study did not account for kerogen pyrolysis or the subsequent flow and extraction of the generated hydrocarbons.

This study aims to develop a comprehensive mathematical model to elucidate the interactions among electric field distribution, temperature distribution, and product flow in oil shale reservoirs subjected to electrical resistance heating. The model considers the electric and thermal fields across the overburden, underburden, and oil shale layers while characterizing the flow behavior of generated hydrocarbons using Darcy′s law for porous media. The numerical solution, obtained via the finite element method, enables the calculation of oil and gas production from in-situ pyrolysis under ERH conditions. Our results confirm the feasibility of ERH for oil shale extraction, demonstrating its superior thermal efficiency compared to conventional conduction heating. This model enhances the theoretical understanding of ERH in in-situ oil shale extraction and provides guidance for optimizing experimental studies and production strategies.

2. Mathematical model

2.1 Electrical field

The electric current flow within the stratum is assumed to satisfy the following conservation equation :

$$\nabla \cdot \vec{J} = 0 \tag{1}$$

where $\vec{J}$ is electrical current density (A/m^2), the relationship between $\vec{J}$ and electrical field intensity $\vec{E}$ (V/m) is written as:

$$\vec{J} = \sigma \vec{E} \tag{2}$$

where σ is the electrical conductivity (S/m) of formation. The relationship between electrical field intensity $\vec{E}$ and electrical potential (V) φ is written as:

$$\vec{\mathrm{E}} = -\nabla\varphi \tag{3}$$

Combining Eqs. (2) and (3) gives:

$$\vec{J} = -\sigma\nabla\varphi \tag{4}$$

Substituting Eq. (4) into Eq. (1) yields the following equation of electrical potential in oil shale reservoir:

$$\nabla \cdot (\sigma\nabla\varphi) = 0 \tag{5}$$

The power generated per unit volume within the formation, known as energy density (W/m³), is defined as the temporal rate of energy output relative to the volume of the formation.

$$Q_E = \vec{J} \cdot \vec{\mathrm{E}} \tag{6}$$

2.2 Chemical reactions

The first-order rate law is employed to describe the reaction rates of each individual reaction:

$$\mathrm{r_j} = \mathrm{k_j} \prod_{\mathrm{i}\in\mathrm{react}} \mathrm{c_i} \tag{7}$$

where, $\mathrm{r_j}$ is the reaction rate of the j-th order reaction (mol/(m^3·s)), $\mathrm{k_j}$ i the reaction rate constant of the j-th order reaction (mol/(m^3 · s)), and $\mathrm{c_i}$ is the concentration of the reactant component i (mol/m^3). Arrhenius proposed the analytical equation of the reaction rate constant as follows[16]:

$$\mathrm{k_j} = \mathrm{A_j}\exp\left(-\frac{\mathrm{E_j}}{\mathrm{R_g T}}\right) \tag{8}$$

where $\mathrm{A_j}$ is the frequency factor of the j-th order reaction(1/s), $\mathrm{E_j}$ is the activation energy of the j-th order reaction(J/mol), $\mathrm{R_g}$ is the gas constant (8.314 J/(mol·K)).

The chemical reaction heat is defined as:

$$Q_C = \sum_j r_j H_j \tag{9}$$

where H_j is the enthalpy of the j-th order reaction (J/mol).

Table 1.Kinetic data for the decomposition reaction of kerogen

	Decomposition reactions	Frequency factor (1/s)	Activation energy (J/ mol)
(1)	Kerogen => 0.279 Heavy Oil +0.143 Light Oil + 0.018 Gas +0.005 Methane + 0.555 Coke1	3×10^{13}	2.259×10^{5}
(2)	Heavy Oil => 0.37 Light Oil +0.156 Gas + 0.03 Methane +0.441 Coke2	1×10^{13}	2.134×10^{5}
(3)	Light Oil => 0.595Gas +0.115Methane + 0.29Coke2	5×10^{11}	2.259×10^{5}
(4)	Coke1 => 0.031 Gas + 0.033Methane + 0.936 Coke2	1×10^{13}	2.259×10^{5}
(5)	Coke2 => 0.003 Gas + 0.033Methane + 0.964 Coke2	5×10^{11}	2.259×10^{5}

This study adopts the reaction model proposed by Burnham and Braun[17]. As illustrated in Table 1, the products of the first-order reaction (kerogen pyrolysis) simultaneously serve as reactants for the secondary reactions, which involve the cracking of heavy and light oils.

2.3 Mass transfer

The pyrolysis of kerogen in a porous medium produces various chemical components, including both solids and fluids. The mass conservation equations for each component are employed to determine their respective concentrations:

$$\frac{\partial(\varepsilon_p c_i)}{\partial t} + \nabla \cdot \vec{J}_i + \vec{u} \cdot \nabla c_i = R_i \tag{10}$$

where c_i is the concentration of component i, $\vec{u}$ is the mass average velocity vector (m/s), R_i is the mass source due to chemical reaction (mol/(m^3·s)), which is obtained from Eq.(7), The variable $\vec{J}_i$ represents the mass flux in relation to the velocity averaged over mass, measured in moles per square meter per second (mol/(m^2 s)).:

$$\vec{J_i} = -D_i \nabla c_i \tag{11}$$

where D_i is the effective diffusion coefficient of component *i* in porous media (m^2/s).

As solid kerogen is decomposed and new solid products are formed, the porosity evolves accordingly. These changes in porosity directly affect the permeability, which, in turn, significantly influences fluid flow through the porous medium. It is important to note that the porosity used in the governing equations refers to the effective porosity ε_p :

$$\varepsilon_p = \varepsilon\left(1 - \sum_{i \in solid} \theta_i\right) \tag{12}$$

where ε is the absolute porosity, θ_i denotes the volume fraction of solid components relative to the absolute porosity.

The velocity $\vec{u}$ appearing in the convective terms of Eq. (10) is governed by Darcy's law:

$$\vec{u} = -\frac{k}{\mu}(\nabla P - \rho_f \vec{g}) \tag{13}$$

where k is the permeability of the oil shale (m^2), μ is the dynamic viscosity of the fluid (kg/(m·s)), and P is the fluid pressure (Pa). The relationship between permeability and porosity in oil shale is established based on the findings of Burnham [18]:

$$k = \frac{30\varepsilon_p^{2.5}}{(1-\varepsilon_p)^2} \tag{14}$$

2.4 Heat transfer

In the energy conservation equation, both heat conduction and heat convection are considered:

$$\rho C_P \frac{\partial T}{\partial t} + \rho_f C_f \vec{u} \cdot \nabla T + \nabla \cdot (-k_{eff} \nabla T) = Q \tag{15}$$

where ρ is the overall density of the formation (kg/m^3), C_P is the specific heat capacity of the formation at constant stress (J/(kg·K)), ρ_f is the density of the fluid (kg/m^3), C_f is the specific heat capacity of the fluid at constant stress(J/(kg · K)), $\vec{u}$ is the velocity of fluid (m/s), k_{eff} is the equivalent thermal conductivity of the formation (W/(m·K)), and Q is the heat source term (W/m^3).

The expression for ρC_P is given by:

$$\rho C_P = \varepsilon_p \rho_f C_f + (1 - \varepsilon_p)\rho_s C_s \tag{16}$$

where ε_p is the porosity of porous medium, ρ_s is the density of the solid(kg/m^3), and C_s is the specific heat capacity of the solid at constant stress (J/(kg·K)).

The equivalent thermal conductivity, k_{eff} is defined as:

$$k_{eff} = \varepsilon_p k_f + (1 - \varepsilon_p)k_s \tag{17}$$

where k_f is the thermal conductivity of mixed fluid in oil shale (W/(m·K)), and k_f is the thermal conductivity of solid (W/(m·K)).

The source term in the energy conservation equation consists of the following two components:

$$Q = Q_E + Q_C \tag{18}$$

where Q_E is the energy density defined in Eq.(6), and Q_C is the reaction heat defined in Eq.(9).

2.5 Numerical solution

This study employs the finite element method to solve four physical fields. In conjunction with the control equations used in the numerical model, the coupling logic illustrated in Fig. 1 is adopted as the solution strategy for the model's numerical resolution.

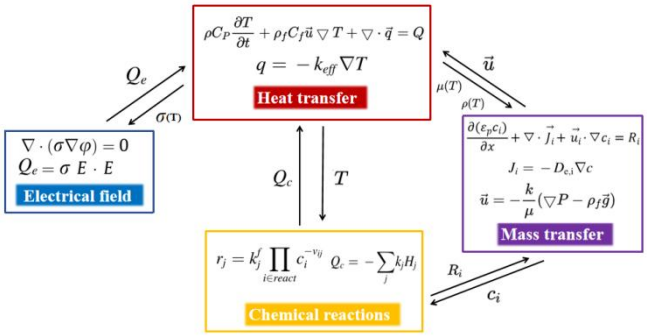

Fig.1 Relationship of physical fields coupling for electrical resistance heating of oil shale

3. Results and discussion

3.1 Reservoir model

In this paper, we develop a three-dimensional physical model to simulate the resistance heating of oil shale using horizontal wells, as shown in Fig. 2. The model represents an oil shale reservoir bounded by overburden and underburden layers, which differ from the reservoir in electrical and thermal conductivities and do not contain kerogen. The geometric model, based on the conceptual diagram in Fig.2, has dimensions of 15 m × 15 m in area and 5 m in height for both the overburden and reservoir layers. Two parallel electrodes, each 10 m long and spaced 9 m apart, are placed in the middle of the reservoir.

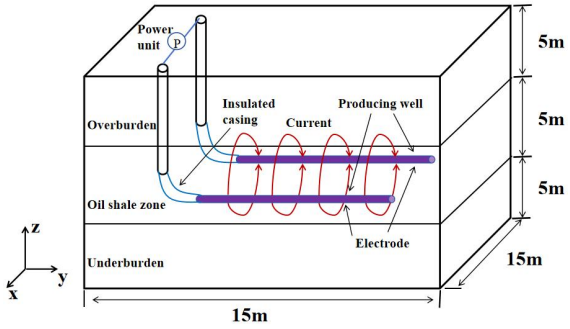

Fig.2 Diagram of electrical resistance heating oil shale reservoir using horizontal electrode wells.

3.2 Numerical result

In this section, a 25kW power source is applied to continuously heat the formation, with the assumption that all electrical energy is entirely converted into heat. Fig.3(a) illustrates the distribution of the electric field within the formation, showing a higher field strength and denser field lines in proximity to the electrodes. Fig.3(b) presents the energy density distribution, which mirrors the pattern of the electric field strength.

The analysis shows that high energy density is concentrated near the electrodes, primarily due to the large potential gradient in this region. As illustrated in Fig.3(c), the energy density is represented by the height, with higher energy densities corresponding to greater heights. This region is the first to experience a temperature increase, and kerogen undergoes pyrolysis earliest in this area.

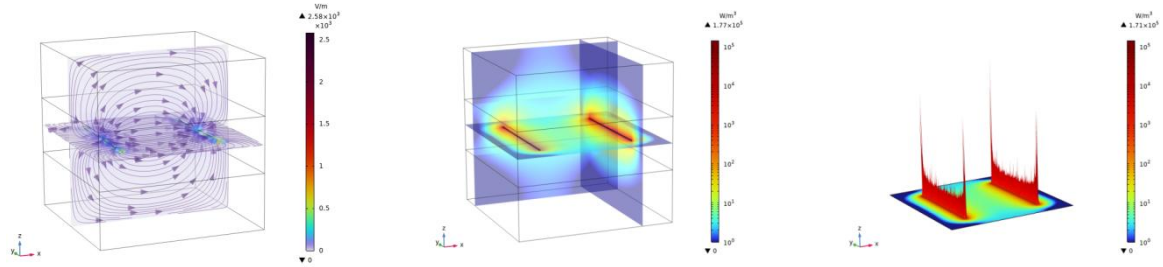

(a)Electric field intensity; (b)Energy density; (c)Energy density of the middle x-y plane.

Fig. 3 Electric field calculation result.

The energy density near the electrodes is high, leading to rapid temperature rise. Fig.4(a) illustrates the temperature distribution on the xy-plane at 200, 400, 600, and 800 days. At 200 days, the formation undergoes initial heating; under the combined effects of thermoelectric conversion and heat conduction, it continues to increase in temperature. By 600 days, most of the region reaches the temperature necessary for kerogen pyrolysis reactions to occur.

The pyrolysis of kerogen is directly influenced by temperature. Once the temperature reaches the reaction threshold, kerogen begins to undergo pyrolysis, resulting in the generation of various hydrocarbons. Fig.4(b) illustrates the distribution of kerogen concentration at four distinct time points on the central horizontal plane, reflecting the same characteristics as the temperature distribution depicted in Fig.4(a).

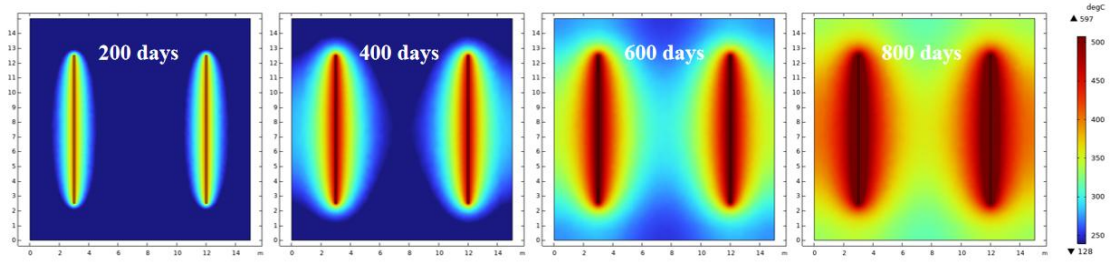

(a)Temperature distribution on the central xy-plane

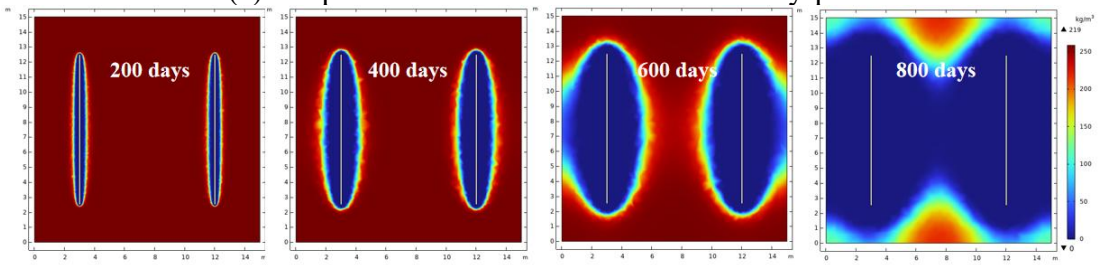

(b)Concentration distribution of kerogen on the xy-plane

Fig.4 Distribution of temperature and kerogen concentration.

By comparing the calculated results of temperature and kerogen concentration, it is evident that significant kerogen consumption occurs in regions where the temperature exceeds 300°C. The reaction temperature is consistent with the experimental phenomena of previous researchers[19].

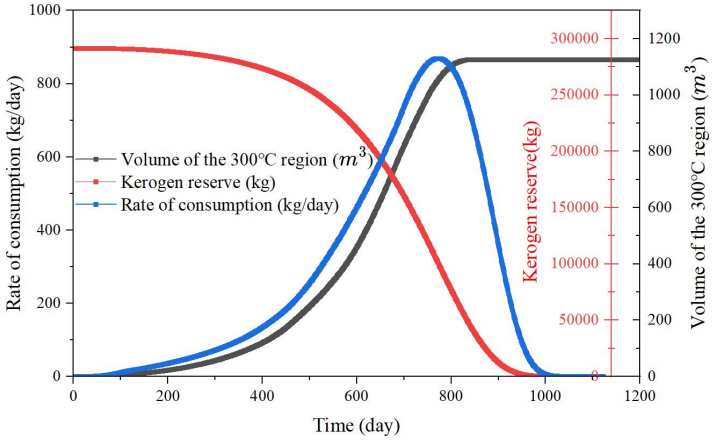

Fig.5 The consumption of kerogen and the volume of heated region.

Fig.5 illustrates the volume of the region where the temperature exceeds 300°C (black curve), as well as the corresponding changes in kerogen reserves (red curve) and the daily rate of kerogen pyrolysis (blue curve). It is evident that as more regions are heated to the reaction temperature, the pyrolysis rate of kerogen rapidly increases. The expansion rate of the heated region and the increase in the pyrolysis rate show a similar trend. By day 800, the entire reservoir has been heated above 300°C, and the pyrolysis rate reaches its peak. According to Eq. (7), the reaction rate is dependent on the concentration of the reactants, and as the kerogen reserves (red curve) gradually decrease, the pyrolysis rate also begins to decline after day.

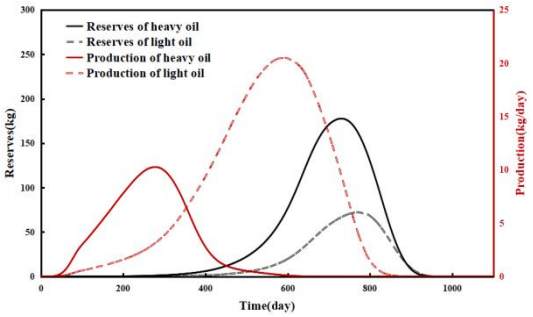

(a)Reserves and production of oil Production rate

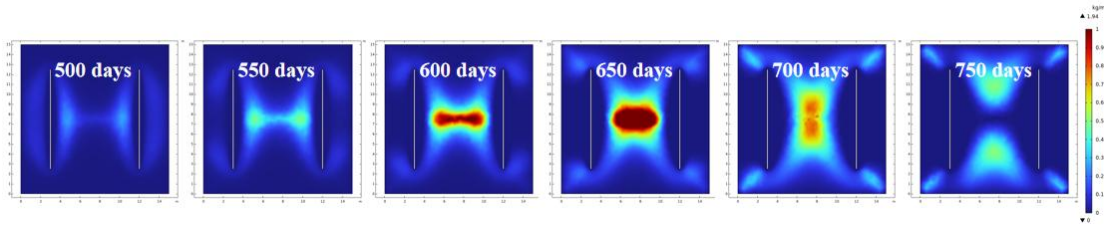

(b) heavy oil concentration distribution

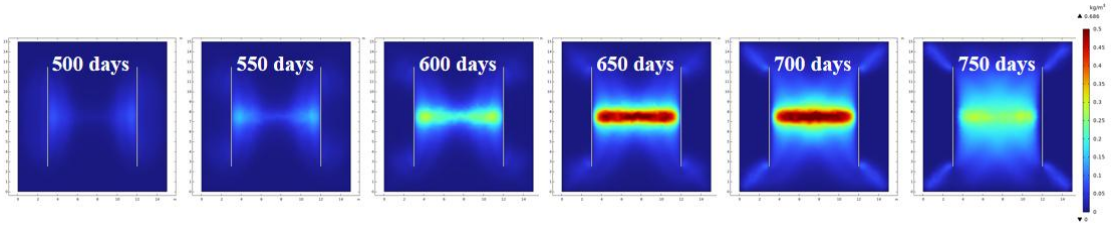

(c) light oil concentration distribution

Fig.6 production of oil.

As kerogen undergoes pyrolysis, various products are continuously generated. Fig.6(a) illustrates the production and reserves of oil products. Combining this with the temperature distribution shown in Fig.4(a), it can be observed that from 1 to 400 days, the areas near the electrodes reach the pyrolysis temperature, leading to significant production of heavy oil during this period. As the heated region expands, kerogen located farther away begins to undergo pyrolysis; however, these areas are too distant from the production wells for timely extraction. The black curve in the figure reflects the reserves of oil products under these circumstances.

Fig. 6(b) shows the concentration distribution of heavy oil, indicating its migration toward the production well. However, its concentration drops sharply near the well due to high temperatures, which accelerate heavy oil cracking. As a result, Fig. 6(c) reveals a corresponding increase in light oil concentration in these regions. This trend is further supported by Fig. 6(a), where light oil production remains high even after heavy oil production ceases, suggesting that light oil is generated not only from direct kerogen pyrolysis but also from heavy oil cracking. After 600 days, light oil production declines while its in-place reserves continue to grow, primarily from kerogen pyrolysis in more distant regions. By 800 days, production ceases, but residual oil remains in the formation and will eventually crack into lighter products.

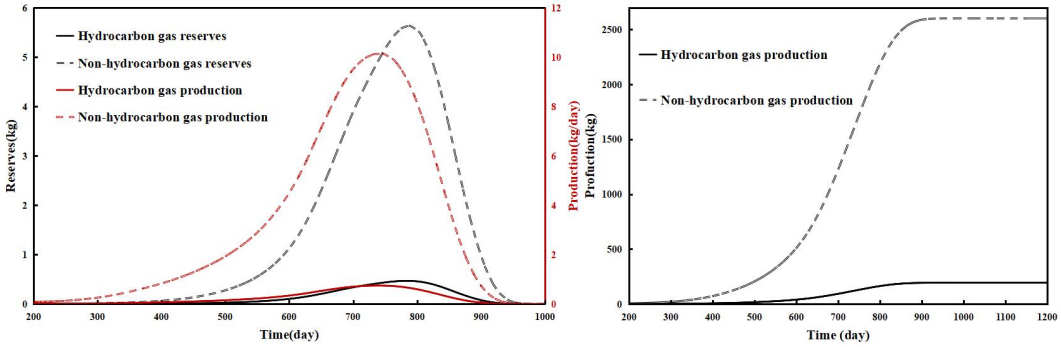

(a) Reserves and production of gas (b)Total production of gas

Fig.7 Production of gas.

Fig.7 illustrates the production of gas products, indicating that the yield and reserves of hydrocarbon gas reach their peak between days 700 and 800. This increase is primarily due to the significant cracking of both heavy oil and light oil during this period. By day 1000, all produced hydrocarbon gas has been fully extracted from the production wells.

4. Summary

This study investigates the feasibility of using electrical resistance heating (ERH) for in-situ oil shale extraction through numerical simulation. A comprehensive mathematical model was developed to integrate the electric field, heat transfer, chemical reactions, and mass transport processes.

The findings highlight the critical role of temperature in influencing the decomposition pathways of kerogen and the subsequent formation of heavy oil, light oil, and gas. The results also confirm that heavy oil undergoes secondary cracking near production wells, contributing to light oil production. Furthermore, the analysis of hydrocarbon migration and reservoir evolution underscores the importance of optimizing electrode placement and heating power to maximize extraction efficiency.

This research provides valuable insights into the theoretical mechanisms of ERH for oil shale extraction and serves as a foundation for further experimental validation and optimization studies. Future work should focus on refining the model by incorporating field-scale conditions, optimizing

heating strategies, and evaluating the long-term economic feasibility of ERH for large-scale deployment in oil shale reservoirs.

References

[1] J. R. Dyni, “Global oil shale resources: An overview,” Energy Fuels, vol. 20, no. 3, pp. 1547–1559, 2006.

[2] B. Jia and J. Su, “Advancements and environmental implications in oil shale exploration and processing,” Appl. Sci., vol. 13, no. 13, p. 7657, 2023.

[3] H. Vinegar, “Shell’s in-situ conversion process,” presented at the 26th Oil Shale Symp., Colorado School of Mines, Golden, CO, USA, Oct. 16–20, 2006.

[4] S. Wang, X. Jiang, X. Han, and J. Tong, “Investigation of Chinese oil shale resources comprehensive utilization performance,” Energy, vol. 42, no. 1, pp. 224–232, 2012.

[5] D.-X. Liu, H.-Y. Wang, D.-W. Zheng, et al., “World progress of oil shale in-situ exploitation methods,” Nat. Gas Ind. (China), vol. 29, no. 5, pp. 128–132, 2009.

[6] Y. Zhang, J. Wang, Y. Chen, et al., “Numerical simulation of microwave heating of oil shale: A comparative study of various heating methods,” J. Nat. Gas Sci. Eng., vol. 46, pp. 353–362, 2017.

[7] J. Zhu, L. Yi, Z. Yang, and M. Duan, “Three-dimensional numerical simulation on the thermal response of oil shale subjected to microwave heating,” Chem. Eng. J., vol. 407, p. 127197, 2021.

[8] T. Ramsay, "Uncertainty quantification of an explicitly coupled multiphysics simulation of in-situ pyrolysis by radio frequency heating in oil shale," SPE Journal, vol. 25, pp. 1443–1461, 2020.

[9] A. Bera and T. Babadagli, "Status of electromagnetic heating for enhanced heavy oil/bitumen recovery and future prospects: A review," Appl. Energy, vol. 151, pp. 206–226, 2015.

[10] H. C. Wang and S. A. Rezaee, "The interaction of reservoir properties and microwave heating – an experimental and numerical modelling study of enhanced gas recovery (EGR)," Procedia Earth Planet. Sci., vol. 15, pp. 542–548, 2015.

[11] W. A. Symington, J. S. Burns, W. El-Rabaa, G. A. Otten, N. Pokutylowicz, P. M. Spiecker, R. W. Williamson, and J. D. Yeakel, "Field testing of Electrofrac™ process elements at ExxonMobil's Colony Mine," in 29th Oil Shale Symposium, Colorado School of Mines, Golden, CO, 2009.

[12] E. J. Martin and B. H. Kueper, "Observation of trapped gas during electrical resistance heating of trichloroethylene under passive venting conditions," J. Contam. Hydrol., vol. 126, pp. 291–300, 2011.

[13] Y. Wang, B. Liao, L. Qiu, et al., "Numerical simulation of enhancing shale gas recovery using electrical resistance heating method," Int. J. Heat Mass Transfer, vol. 128, pp. 1218–1228, 2019.

[14] Y. Pan, J. Peng, S. Yang, J. Fu, and L. Li, "Review of electric heating technology of oil shale and its simulation," J. Anal. Appl. Pyrolysis, vol. 175, p. 106205, 2023.

[15] H. Yang, et al., "Temperature distribution simulation and optimization design of electric heater for in-situ oil shale heating," Oil Shale, vol. 31, no. 2, 2014.

[16] Y. Fan, L. J. Durlofsky, and H. A. Tchelepi, "Numerical simulation of the in-situ upgrading of oil shale," SPE J., vol. 15, no. 2, pp. 368–381, 2010.

[17] A. Burnham and R. Braun, "Pmod: A flexible model of oil and gas generation, cracking, and expulsion," Org. Geochem., vol. 19, pp. 167–172, 1992.

[18] A. K. Burnham, "Porosity and permeability of Green River oil shale and their changes during retorting," Fuel, vol. 203, pp. 208–213, 2017.

[19] J. G. Na, C. H. Im, S. H. Chung, and K. B. Lee, "Effect of oil shale retorting temperature on shale oil yield and properties," Fuel, vol. 95, pp. 131–135, 2012.